Green Chemistry

Cite this: *Green Chem.*, 2012, **14**, 1086

www.rsc.org/greenchem

PAPER

Chemoselective reduction of a nitro group through transfer hydrogenation catalysed by Ru^0-nanoparticles stabilized on modified Montmorillonite clay

Podma Pollov Sarmah and Dipak Kumar Dutta*

Received 11th November 2011, Accepted 30th January 2012
DOI: 10.1039/c2gc16441h

Ru^0-nanoparticles of approximately 5 nm size were generated by incipient impregnation of $RuCl_3$ into the nanopores of the acid activated Montmorillonite clay followed by polyol reduction. Acid activation of the clay increases the surface area by generating nanopores (0–10 nm), which act as a host and stabilize nanoparticles in the pores. The generated Ru^0-nanoparticles exhibit inter-planar lattice fringe spacing of 0.21 nm of the face centered cubic lattice of Ru^0 crystals, and show efficient catalytic activity in the chemoselective transfer hydrogenation reduction of substituted nitrobenzenes to corresponding anilines with high yield of conversion (56–97%) and selectivity (91–100%) depending upon the nature of the substituents. The reactions were carried out in the presence of isopropanol, which served as the solvent as well as the reductant. The catalysts were found to be active for several catalytic runs.

1. Introduction

Supported metals are useful as heterogeneous catalysts in a wide variety of organic transformation.[1–4] Nanoparticles, in comparison to bulk solids, have a significantly high catalytic activity and exhibit novel characteristics of quantum size effects.[4,5] Heterogeneous catalysts are also in great demand for clean technology and sustainable development. Among these, platinum group metals have special importance in chemistry due to their wide spread applications in catalysis, forming the backbones of various important industries. Stabilized and dispersed Ru^0-nanoparticles exhibit high catalytic activity in a wide range of organic reactions, including hydrogenation, oxidation, C–C coupling and related reactions.[7–9] While nanoparticles are very active, they tend to agglomerate to form large particles, leading to loss in activity. To prevent the agglomeration, various stabilizers or supports are used[6,10–12] and a good stabilizer is one that can prevent the particle aggregation and control particle size but does not passivate the nanoparticle surface. The stabilizer or support also plays an important role in controlling the morphology, distribution as well as the activity of the synthesized nanomaterials. Controlled and precise growth of nanoparticles with the desired shape and size can be tuned by altering the morphology of the support. Recently, porous substances with a large internal surface area like Montmorillonite clay (Mont) minerals, zeolites, charcoals containing nanosize channels, *etc.* have been used for the stabilization of metal nanoparticles.[4,6,13–18]

Materials Science Division, CSIR-North East Institute of Science and Technology, Jorhat 785006, Assam, India. E-mail: dipakkrdutta@yahoo.com; Tel: +91 376 2370081; Fax: +91 376 2370011

The reduction of substituted nitrobenzenes to the corresponding anilines is industrially important because anilines are important intermediates for the synthesis of organic fine chemicals, dyes, biologically active compounds, pharmaceuticals, rubber, photographic and agricultural chemicals.[19–23] The traditional synthesis routes for reduction of nitrobenzenes proceeds through catalytic hydrogenation, electrolytic reduction, metal mediated reductions *etc.*[19] But these process mainly utilize potentially explosive H_2 gas, high pressure reactors, hazardous and harmful materials like mineral acids *etc.* In general, the reduction of a nitro group by hydrogen gas is carried out at a moderately high pressure (10–50 bar)[24–26,28] and temperature (100–150 °C),[26,28] which lead to low selectivity (less than 70%) due to non-selective hydrogenation of other functional groups.[28] However, transfer hydrogenation is advantageous over the traditional hydrogenation reaction in respect of selectivity in which an alcohol like isopropanol, considered as one of the green solvents, acts as solvent as well as the source of hydrogen and the reaction takes place at atmospheric pressure and relatively low temperature.[19,27–30] Moreover, the co-production of acetone in the reaction is also a useful chemical and its production is energetically more economical than the commercial 'cumene peroxide' process, which requires high pressure (30 bar) and temperature (250 °C) and is also associated with distillation.[31] The co-produced acetone can be easily isolated by distillation, which makes the whole process 'green'. Here we report the synthesis of Ru^0-nanoparticles of less than 5 nm size into the nanopores of acid activated Montmorillonite (AT-Mont) clay and their application as a catalyst in the transfer hydrogenation of substituted nitrobenzenes to the corresponding anilines with high activity and selectivity.

2. Experimental

2.1 Materials and methods

Bentonite (procured from Gujarat, India) containing quartz, iron oxide *etc.* as impurities was purified by sedimentation technique to collect the <2 μm fraction before use.[32] The basal spacing (d_{001}) of the air dried samples was about 12.5 Å. The specific surface area determined by N_2 adsorption was 101 m^2 g^{-1}. The analytical oxide composition of the bentonite determined was SiO_2: 49.42%; Al_2O_3: 20.02%; Fe_2O_3: 7.49%; MgO: 2.82%; CaO: 0.69%; loss on ignition (LOI): 17.51%; and others (Na_2O, K_2O and TiO_2): 2.05%. Mont was converted to the homoionic Na-exchanged form by stirring in 2 M NaCl solution for about 48 h, washed and dialysed using deionized distilled water until the conductivity of the water approached that of distilled water. The cation exchange capacity (CEC) was 126 milliequivalent (meq) per 100 g of clay (sample dried at 120 °C). $RuCl_3$, ethylene glycol, isopropanol and substrates were purchased from Sigma-Aldrich, USA. All reagents were used as supplied.

IR spectra (4000–400 cm^{-1}) were recorded on KBr discs in a Shimadzu IR Affinity-1 spectrophotometer. Powder XRD spectra were recorded on a Rigaku Ultima IV from 2–80° 2θ using a CuKα source (λ = 1.54 Å). Specific surface area, pore volume, average pore diameter were measured with the Autosorb-1 (Quantachrome, USA). Specific surface area of the samples was measured by adsorption of nitrogen gas at 77 K and applying the Brunauer–Emmett–Teller (BET) calculation. Prior to adsorption, the samples were degassed at 250 °C for 3 h. Pore size distributions were derived from desorption isotherms using the Barrett–Joyner–Halenda (BJH) method.[33,34] The ^1H NMR spectra were recorded at room temperature in $CDCl_3$ solution on a Bruker DPX-300 spectrometer and chemical shifts were reported relative to $SiMe_4$. Mass spectra were recorded on ESQUIRE 3000 mass spectrometer. Scanning electron microscopy (SEM) images and energy dispersive X-ray spectroscopy (EDX) patterns were obtained by Leo 1430 vp operated at 3 and 10 kV on a gold coated sample. Transmission electron microscopy (TEM) and high resolution transmission electron microscopy (HR-TEM) images were recorded on a JEOL JEM-2011 electron microscope and the specimens were prepared by dispersing powdered samples in isopropyl alcohol, placing them on a carbon coated copper grid and allowing them to dry. X-ray photoelectron spectra were recorded on Kratos ESCA model Axis 165 spectrophotometer having a position sensitive detector and hemispherical energy analyzer in an ion pumped chamber.

2.2 Support preparation

Purified Mont (10 g) was dispersed in 200 mL 4 M hydrochloric acid and refluxed for 1 h. After cooling, the supernatant liquid was discarded and the acid activated Mont was repeatedly redispersed in deionized water until no Cl^- ions could be detected by the $AgNO_3$ test. The modified Mont was recovered, dried in air at 50 ± 5 °C overnight to obtain the solid product. The acid activated Mont was designated as AT-Mont.

2.3 Ru^0-nanoparticles preparation

1 g AT-Mont was impregnated by 15 mL aqueous solution of $RuCl_3$ (0.50 mmol) under vigorous stirring conditions. Stirring was continued for another 12 h before the mixture was evaporated to dryness in a rotavap. 0.5 g of the dry composite was dispersed in 20 mL ethylene glycol solution and refluxed at 178 °C for 5–6 h and the colour of the solid changed from reddish purple to black. The solid was allowed to settle and washed with distilled water several times. Finally the solution was filtered through a sintered crucible and washed with methanol and then with distilled water. The composite was collected and dried at 60 °C for 12 h and stored in an airtight bottle. The samples thus prepared were designated as Ru^0-AT-Mont.

2.4 Catalytic transfer hydrogenation reaction

0.2 mmol of the reactant was dissolved in 20 mL isopropanol followed by addition of 50 mg of Ru^0-AT-Mont and 20 mg

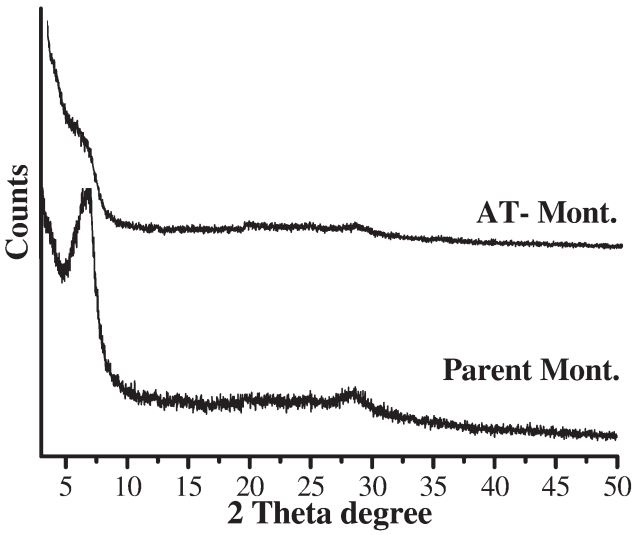

Fig. 1 Powder XRD patterns of Mont and AT-Mont.

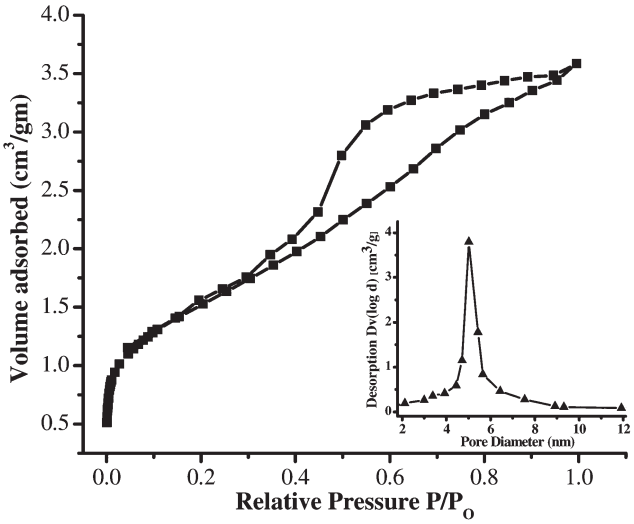

Fig. 2 N_2 adsorption–desorption isotherm and BJH pore size distribution curve of AT-Mont.

NaOH (0.5 mmol) to a 100 mL round bottom flask. The reaction mixture was refluxed at 82 °C for the desired time period under a nitrogen atmosphere. To investigate the recyclability, the used catalyst was filtered after the reaction and vacuum-dried at 150 °C before the next reaction run. The product mass along with the reactant were separated from the reaction mixture by evaporating the solvent in a rotavap. The mixture of solvents (acetone and isopropanol) thus obtained were fractionally distilled to obtained the pure solvents. The yields of the products were calculated by separating the individual components by column chromatography and the products were identified by using mass spectrometry and ^{1}H NMR spectroscopy.

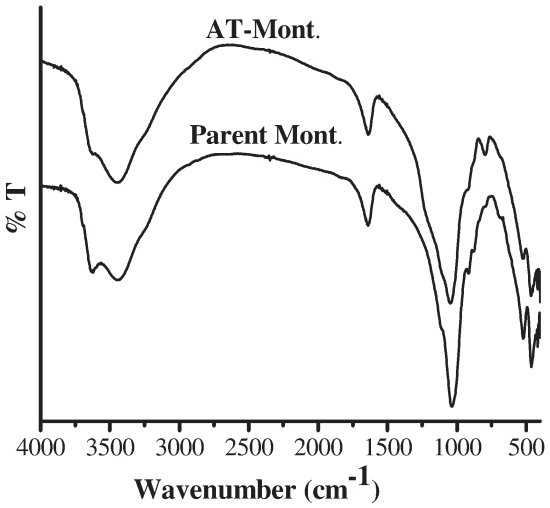

Fig. 3 FT-IR spectra of parent and acid AT-Mont.

3. Results and discussion

3.1 Characterization of the modified support

The powder XRD (Fig. 1) of the parent Mont shows an intense reflection at $2\theta = 7.06°$ corresponding to a basal spacing (d_{001}) of 12.5 Å while in AT-Mont, the reflection almost vanishes, indicating depletion of the lamellar structure.[30] The CEC of the purified natural Mont decreases from 126 to 40.8 meq per 100 g of clay upon acid activation for 1 h. The surface area and pore size distribution of the AT-Mont determined by N_2-adsorption study reveals that AT-Mont contain both micro and mesopores with average pore diameters of 5 nm and exhibits high specific surface area of about 580 m^2 g^{-1} with large specific pore volumes of 0.60 cm^3 g^{-1}. Acid activation modifies the layered structure of Mont by leaching out aluminum from octahedral sites thereby creating a porous matrix with a high surface area. The adsorption–desorption isotherms (Fig. 2) were of the type IV with a H3 hysteresis loop at $P/P_0 \sim 0.4$–0.9, indicating mesoporous solids. The BJH pore size distribution plot (Fig. 2) indicates a relatively narrow pore size distribution with a peak pore diameter centered within 4 to 6 nm. IR study (Fig. 3) reveals that the parent Mont exhibits an intense absorption band at 1034 cm^{-1} for Si–O stretching vibrations of a tetrahedral sheet and also shows broad absorption bands at 3633 cm^{-1} due to

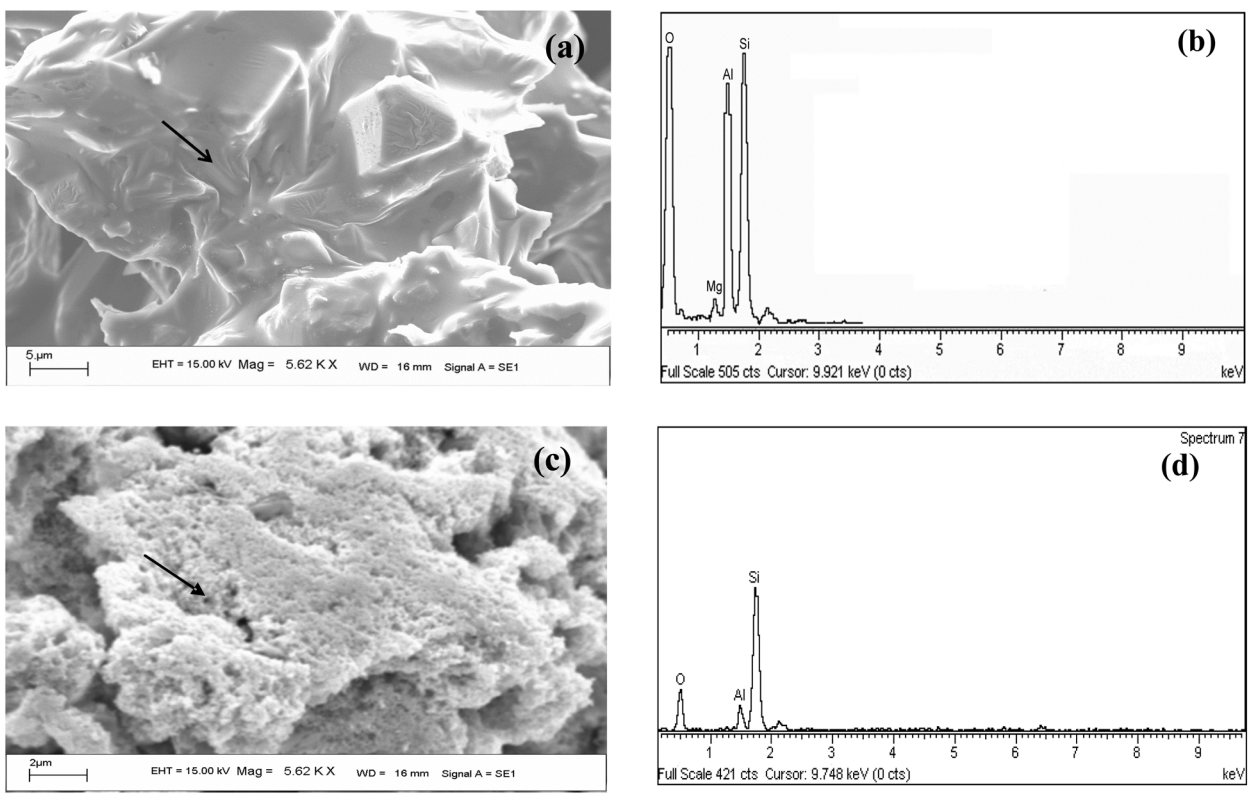

Fig. 4 (a) A SEM image of Mont, (b) EDX analysis of Mont, (c) a SEM image of AT-Mont, (d) EDX analysis of AT-Mont.

stretching vibrations of –OH groups of Al–OH.[35] The bands at 522 and 460 cm^{-1} are due to Si–O–Al and Si–O–Si bending vibrations mode, respectively. Upon acid activation, the Si–O stretching vibration band shifts from 1034 to 1083 cm^{-1}, indicating the change in bonding environment surrounding the tetrahedral sheet. The typical SEM image of Mont and AT-Mont (Fig. 4 (a) and 4(c)) indicate the formation of porous surface on Mont upon acid treatment which is not observed on untreated one. The EDX patterns of (Fig. 4(b) and 4(d)) show a decrease in Al content upon acid activation that clearly indicates the leaching of aluminum from the clay structure.

3.2 Characterization of supported Ru^0-nanoparticles

Evidence for the formation of Ru^0-nanoparticles was obtained from powder XRD analysis (Fig. 5) wherein a broad peak centered at $2\theta = 43.7°$ can be assigned to the (101) reflection of hexagonal close-packed Ru^0, which is consistent with the standard ruthenium metal data.[5,11] Using Scherrer formula,[36] the average size of the supported Ru^0-nanoparticles was estimated to be about 3.2 nm. The binding energies of the supported Ru^0-nanoparticles shown in the XPS spectrum (Fig. 6(a) and 6(b)) bands at 281.4, 285.6 and 462.8 eV, assigned to Ru^0 $3d_{5/2}$, $3d_{3/2}$, and $3p_{3/2}$, respectively, which are of slightly higher values by 1.4, 0.6, and 1.8 eV, respectively, than those of the free ruthenium metal and therefore confirming the formation of metallic particles. These higher values may be attributed to the interaction of Ru^0-nanoparticles with the framework oxygen of the clay matrix, which is expected to induce a positive charge on the metal surface and thereby increasing the binding energies of Ru^0-nanoparticles.[37] The morphology of the supported Ru^0-nanoparticles were investigated by TEM and HR-TEM analysis (Fig. 7 and 8) and the sizes of the Ru^0-nanoparticles were found to be below 5 nm, which is in good agreement with the calculated powder XRD data. The particle size histogram (Fig. 7 (inset)) shows a narrow size distribution between 2–7 nm of the synthesized nanoparticles particles. HR-TEM images of a single Ru^0-nanoparticle (Fig. 8) showed the reticular lattice planes inside the nanoparticles. The lattice planes continuously extended throughout the whole particles without stacking faults or twins, indicating the single crystalline nature. The measured inter-planar lattice fringe spacing is about 0.21 nm, which corresponds to the (101) plane of face centered cubic (fcc) Ru^0 crystals. The corresponding selected area electron diffraction (SAED) pattern of Ru^0-nanoparticles obtained by focusing the electron beam on the nanoparticle lying on the TEM grid is shown in Fig. 8 (inset). The formation of hexagonal symmetrical diffraction spot patterns indicates that the generated Ru^0-nanoparticles are in fact of monocrystalline nature. The specific surface area measurement of the Ru^0-nanoparticles supported on AT-Mont (N_2-adsorption) reveals that the value remarkably decreases to 327 from 580 $m^2\ g^{-1}$, which indicates the generation of the Ru^0-nanoparticles inside the pores on the clay matrix, resulting in decrease of surface area. The Ru content in the Ru^0-AT-Mont was estimated using ICP-AES, which

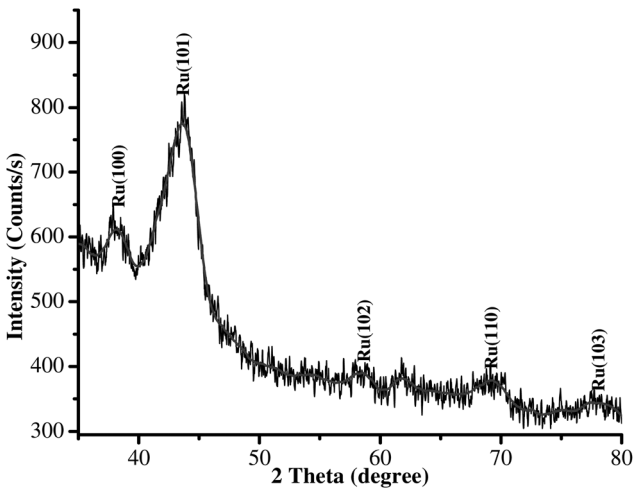

Fig. 5 The powder XRD pattern of Ru^0-nanoparticles supported on AT-Mont.

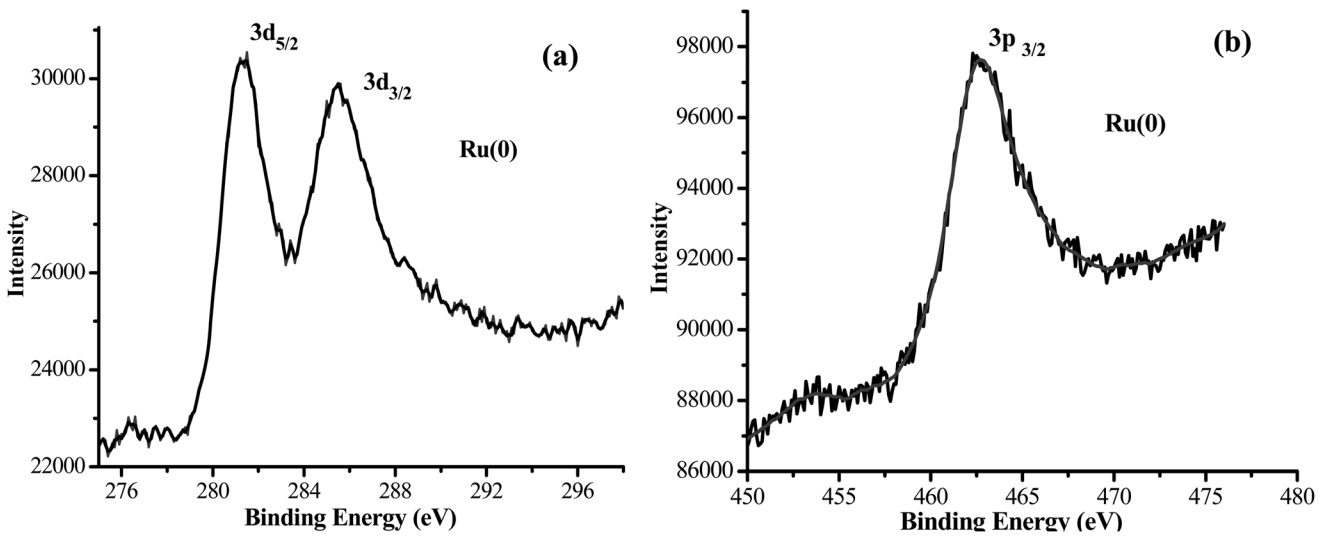

Fig. 6 (a) and (b) XPS analysis of Ru^0-nanoparticles supported on AT-Mont.

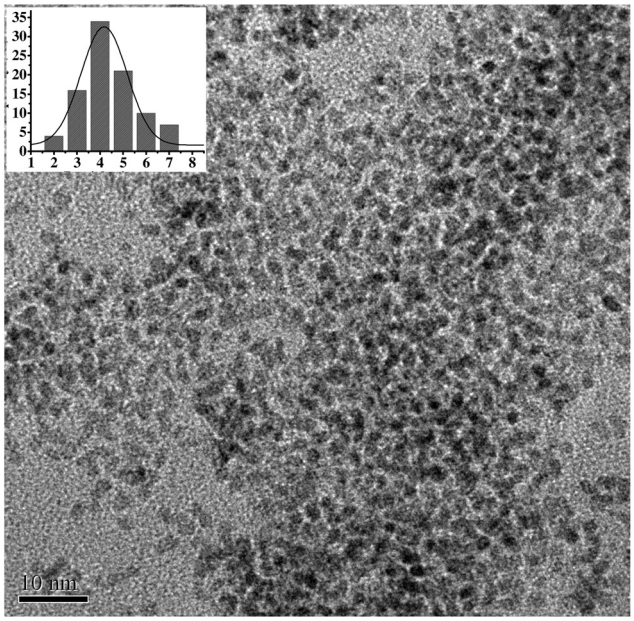

Fig. 7 A TEM image and particle size histograms with a Gaussian curve fitting (inset) of Ru^0-nanoparticles on AT-Mont.

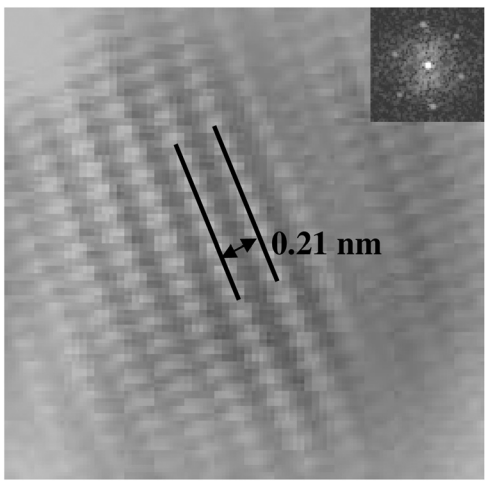

Fig. 8 A HRTEM image and corresponding SAED pattern (inset) of Ru^0-nanoparticles on AT-Mont.

shows the presence of 0.048 mol of Ru per 100 g of the nanocomposite.

3.3 Catalytic transfer hydrogenation

The Ru^0-nanoparticles stabilized on modified clay were tested as a heterogeneous catalyst in transfer hydrogenation of some important substituted nitrobenzenes to the corresponding anilines (Scheme 1). There are several reports of reduction of substituted nitrobenzenes to the corresponding anilines[19–23,38] but, only a few reactions were carried out through transfer hydrogenation.[19,28] The results of the present study are presented in Table 1. The yields of conversion of some selected substituted

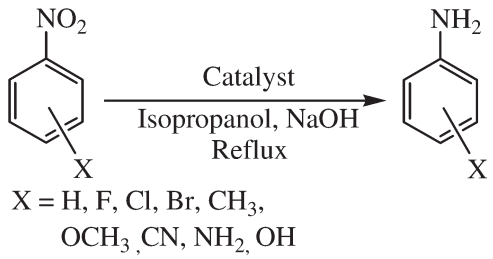

Scheme 1 Hydrogenation of nitrobenzenes to amines in the presence of supported Ru^0-nanoparticles as catalyst.

nitrobenzenes by Ru^0-nanoparticles are found up to 98% with 100% selectivity. However, a control reaction with AT-Mont without the presence of Ru did not show any catalytic activity. The lower selectivity of entry 2, 3 and 6 (Table 1) was observed due to the partial dehalogenation to form aniline. Also, the lower selectivity of the product 4-aminobenzonitrile (entry 11, Table 1) may be due to partial reduction of the nitrile group to form the aminomethyl derivative, as identified spectroscopically.

The kinetics of the reaction were also studied. Typical curves of conversion of nitrobenzene to aniline catalysed by fresh, as well as recovered, catalyst are shown in Fig. 9. The reactant *versus* time plot indicates that the reaction proceeds initially with rapid decrease of reactant concentration up to about 4 h, but later on, it follows almost first order reaction kinetics. Recyclability tests of the catalyst were carried out on the hydrogenation of *p*-chloro nitrobenzene, reusing the recovered catalyst up to three times (Table 1). The catalyst was recovered by simple filtration and vacuum dried at 150 °C before using in the next run. The reactions were carried out by maintaining the stoichiometry of reactant and recovered catalyst. Results show that the catalyst remains active for several runs without significant lost in efficiency. The recovered catalyst was further investigated through N_2 adsorption–desorption study (Fig. 10a), powder XRD (Fig. 11) and TEM analysis (Fig. 12). The specific surface area of the recovered catalysts decrease marginally to 297 (2nd run) and 283 $m^2\ g^{-1}$ (3rd run) compared to 327 $m^2\ g^{-1}$ of freshly prepared catalyst. The decrease of the surface area of the catalyst after reaction may be due to the partial destruction of the support by the small amount of base used in the reaction. It was observed that the adsorption–desorption hysteresis loop of the catalyst used in the 1st run ranging between $P/P_0 = 0.4$ and 0.9 shifted to $P/P_0 = 0.6$ and 1.0, respectively. This may be due to the change in the structure of pores. The BJH pore size distribution curve (Fig. 10(b)) of the recovered catalyst shows a slight broadening of the distribution pattern compared to fresh catalyst, indicating breakdown of the pore walls forming larger pores. However, the recovered catalyst showed almost the same powder XRD pattern like the fresh catalyst. TEM image confirms that the Ru^0-nanoparticles were still inside the clay matrix but some of the particles agglomerated to form bigger size. The Ru content in the recovered catalyst after the 3rd run was estimated using ICP-AES, which show the presence of 0.046 mol Ru per 100 g of the catalyst. This indicated that only very small amounts of Ru^0-nanoparticles are leaching out from the clay matrix.

Table 1 Results of the transfer hydrogenation reaction of substituted nitrobenzenes to the corresponding anilines catalyzed by Ru^0-nanoparticles supported on AT-Mont

Entry	Substrate	Product	Reaction time (h)	Yield (%)	Selectivity (%)
1	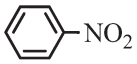	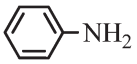	12	97	100
2	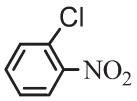	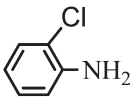	12	83	91
3	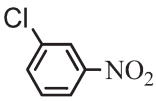	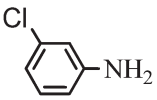	12	76	94
4	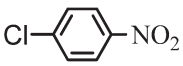	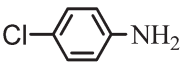	12	91 (1st run) 87 (2nd run) 86 (3rd run)	100
5	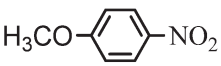	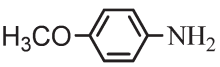	6	56	100
6	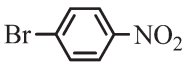	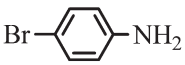	12	84	88
7	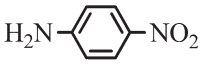	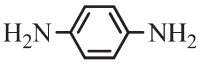	12	78	100
8	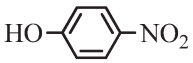	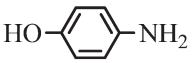	12	65	100
9	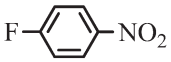	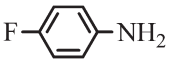	12	54	100
10	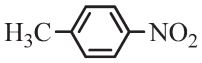	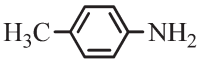	4	98	100
11	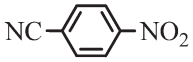	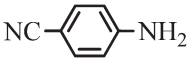	12	78	89
12	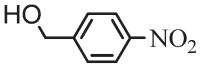	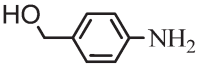	5	98	100

4. Conclusion

The surface area and pore volume as well as pore size distribution of the Mont were modified to mesoporous range by acid activation. Ru^0-nanoparticles of size below 5 nm are synthesized into the nanopores by impregnating $RuCl_3$ into the pores of the acid activated Mont followed by polyol reduction. Electron microscopy as well as other analytical techniques confirm the formation of Ru^0-nanoparticles. The synthesized Ru^0-nanoparticles show high activity and selectivity in the transfer hydrogenation of substituted nitrobenzenes to the corresponding anilines. The catalyst is also found to remain active for several runs without significant loss in activity.

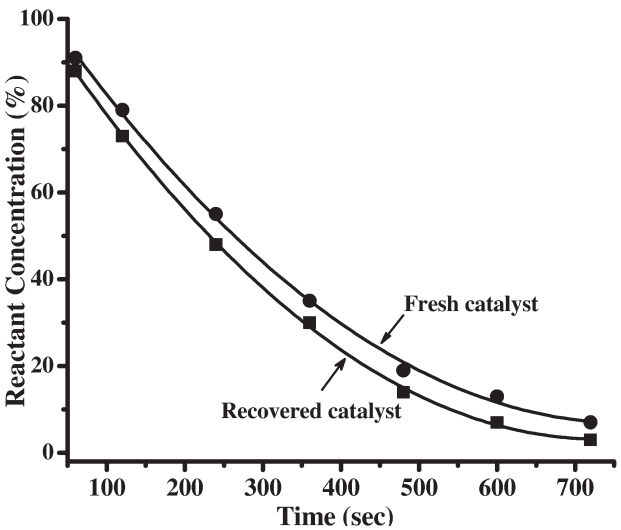

Fig. 9 Kinetic plots of the conversion of nitrobenzene to aniline *versus* time.

Acknowledgements

The authors are grateful to Dr P. G. Rao, Director, CSIR-North East Institute of Science and Technology, Jorhat, Assam, India, for his kind support and permission to publish the work. The authors thank Dr P. Sengupta, Head, Materials Science Division, NEIST, Jorhat, for his constant encouragement. Thanks are also due to CSIR, New Delhi for a financial support (Network project no. NWP-0010) and concept of XII FYP Project: Chemical Cluster. The authors PPS is grateful to CSIR for providing the Senior Research Fellowship.

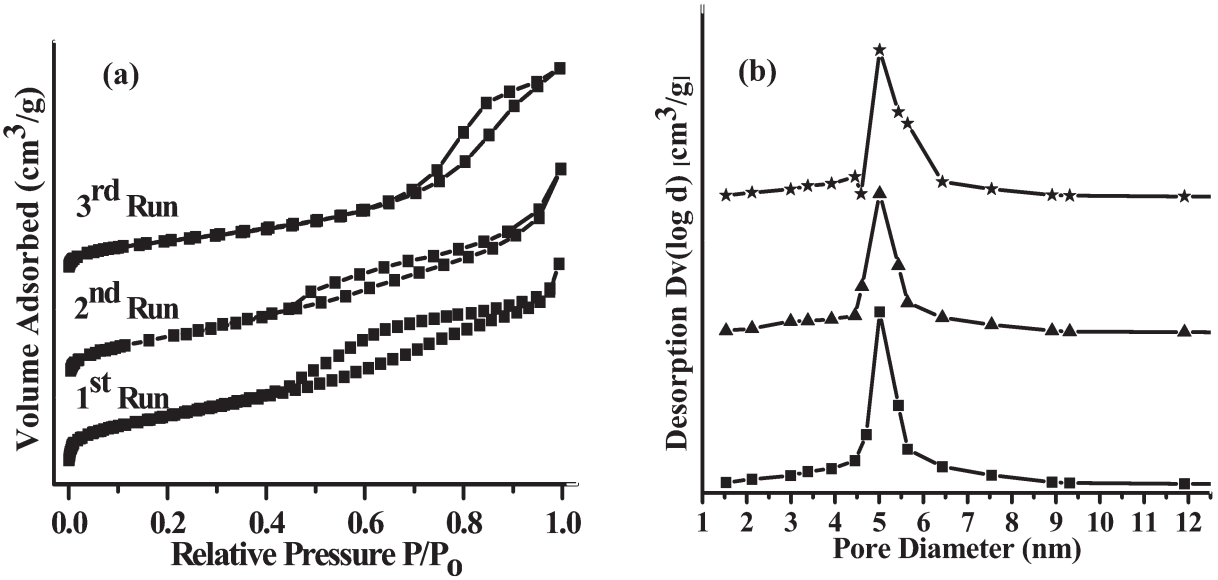

Fig. 10 The stacking pattern of (a) N_2 adsorption–desorption curves and (b) BJH pore distribution curves of fresh and recovered catalysts.

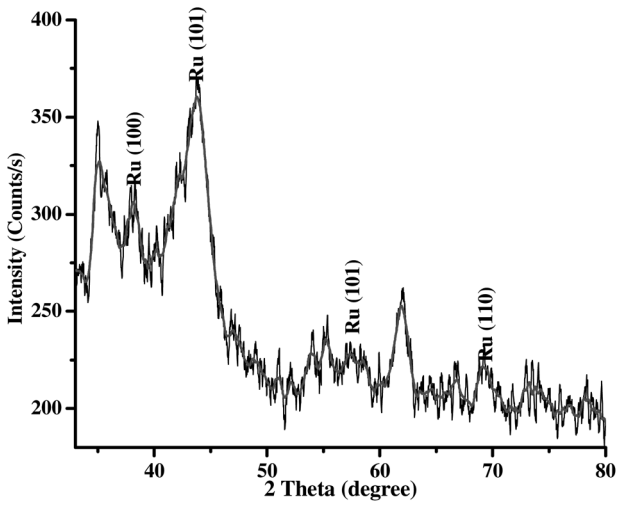

Fig. 11 The powder XRD pattern of recovered catalyst (Ru^0-nanoparticles supported on AT-Mont).

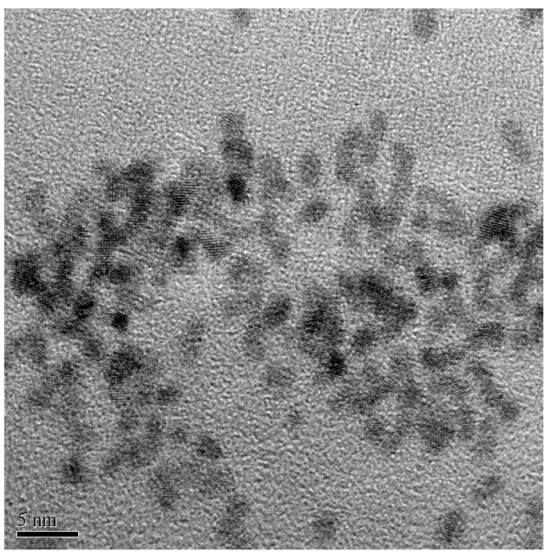

Fig. 12 A TEM image of the recovered catalyst after the 3rd run (Ru^0-nanoparticles supported on AT-Mont).

References

1 C. N. R. Rao, G. U. Kulkarni, P. J. Thomas and P. P. Edwards, *Chem. Soc. Rev.*, 2000, **29**, 27–35.
2 *Nanostructure Science and Technology*, ed. B. Zhou, S. Hermans and G. A. Somorjai, Springer, 2004, vol. 1–3.
3 *Nanotechnology Assessment and Prospectives*, ed. G. Schmid *et al.*, Springer, 2006.
4 H. Bönnemann, W. Brijoux, R. Brinkmann, m. Feyer, W. Hofstadt, G. Khelashvili, N. Matoussevitch and K. Nagabhushana, Nanostructured transition materials, *The Strem Chemiker*, 2004, vol. **XXI**, No. (1).
5 F. Su, L. Lv, F. Y. Lee, T. Liu, A. I. Cooper and X. S. Zhao, *J. Am. Chem. Soc.*, 2007, **129**, 14213–14223.
6 B. J. Borah, D. Dutta and D. K. Dutta, *Appl. Clay Sci.*, 2010, **49**, 317–323.
7 Y. Na, S. Park, S. B. Han, H. Han, S. Ko and S. Chang, *J. Am. Chem. Soc.*, 2004, **126**, 250–258.
8 B. Baruwati, V. Polshettiwar and R. S. Varma, *Tetrahedron Lett.*, 2009, **50**, 1215–1218.
9 M. Takasaki, Y. Motoyama, K. Higashi, S. H. Yoon, I. Mochida and H. Nagashima, *Chem.–Asian J.*, 2007, **2**, 1524–1533.
10 J. D. Aiken and R. G. Finke, *J. Am. Chem. Soc.*, 1999, **121**, 8803–8810.
11 F. Schröder, D. Esken, M. Cokoja, M. W. E. van den Berg, O. I. Lebedev, G. V. Tendeloo, B. Walaszek, G. Buntkowsky, H. H. Limbach, B. Chaudret and R. A. Fischer, *J. Am. Chem. Soc.*, 2008, **130**, 6119–6130.
12 T. Tsukatani and H. Fujihara, *Langmuir*, 2005, **21**, 12093–12095.
13 O. S. Ahmed and D. K. Dutta, *Langmuir*, 2003, **19**, 5540–5541.
14 O. S. Ahmed and D. K. Dutta, *Thermochim. Acta*, 2003, **395**, 209–216.
15 P. B. Malla, P. Ravindranathan, S. Komarneni and R. Roy, *Nature*, 1991, **351**, 555–557.
16 B. J. Borah, D. Dutta, P. P. Saikia, N. C. Barua and D. K. Dutta, *Green Chem.*, 2011, **13**, 3453–3460.
17 D. Manikandan, D. Divakar, A. R. Valentine, S. Revathi, M. E. L. Peethi and T. Sivakumar, *Appl. Clay Sci.*, 2007, **37**, 193–200.
18 D. K. Dutta, D. Dutta, P. P. Sarmah, S. K. Bhorodwaj and B. J. Borah, *J. Biomed. Nanotechnol.*, 2011, **7**, 76–77.

19 S. U. Sonavane, M. B. Gawande, S. S. Deshpande, A. Venkataraman and R. V. Jayaram, *Catal. Commun.*, 2007, **8**, 1803–1806.
20 X. Yuan, N. Yan, C. Xiao, C. Li, Z. Fei, Z. Cai, Y. Kou and P. J. Dyson, *Green Chem.*, 2010, **12**, 228–233.
21 M. Takasaki, Y. Motoyama, K. Higashi, S. H. Yoon, I. Mochida and H. Nagashima, *Org. Lett.*, 2008, **10**, 1601–1604.
22 F. Wang, J. Liu and X. Xu, *Chem. Commun.*, 2008, 2040–2042.
23 A. Corma, P. Serna, P. Concepción and J. J. Calvino, *J. Am. Chem. Soc.*, 2008, **130**, 8748–8753.
24 L. Chen and Y. Chen, *Ind. Eng. Chem. Res.*, 2006, **45**, 8866–8873.
25 M. Lin, B. Zhao and Y. Chen, *Ind. Eng. Chem. Res.*, 2009, **48**, 7037–7043.
26 H. Liu, J. Deng and W. Li, *Catal. Lett.*, 2010, **137**, 261–266.
27 R. Noyori and S. Hashiguchi, *Acc. Chem. Res.*, 1997, **30**, 97–102.
28 M. M. Dell'Anna, V. Gallo, P. Mastrorilli and G. Romanazzi, *Molecules*, 2010, **15**, 3311–3318.
29 T. T. H. Vu, P. S. Kumbhar and F. Figueras, *Adv. Synth. Catal.*, 2003, **345**, 493–496.
30 E. Yilgor, G. E. Atilla, A. Ekin, P. Kurt and I. Yilgor, *Polymer*, 2003, **44**, 7787–7793.
31 S. Sifniades, A. B. Levy and H. Bahl, *Ullmann's Encyclopedia of Industrial Chemistry*, Wiley-VCH, 7th edn, 2011, vol. 1, p257.
32 J. E. Gillott, *Clay in Engineering Geology*, Elsevier, Amsterdam, 1st edn, 1968, ch. 5.
33 F. Rouquerol, J. Rouquerol and K. Sing, *Adsorption by Powders and Porous Solid, Principles, Methodology and Application*, Academic Press, 1999, pp. 191–213.
34 R. M. A. Roque-Malherbe, *Adsorption and Diffusion in Nanoporous Materials*, CRC Press, 2007.
35 P. J. Wallis, W. P. Gates, A. F. Patti, J. L. Scott and E. Teoh, *Green Chem.*, 2007, **9**, 980–986.
36 E. Roduner, *Nanoscopic Materials Size Dependent Phenomena*, RSC Publishing, 2005, p. 11.
37 M. Zahmakiran and S. Özkar, *Langmuir*, 2009, **25**, 2667–2678.
38 G. Fang, L. Junhua and X. Xianlun, *Gongye Cuihua*, 2009, **17**, 49–52.